Structure and dynamics of electrical double layers in organic electrolytes†

Guang Feng,[a] Jingsong Huang,[b] Bobby G. Sumpter,[b] Vincent Meunier[b] and Rui Qiao*[a]

Received 8th January 2010, Accepted 25th February 2010
First published as an Advance Article on the web 30th March 2010
DOI: 10.1039/c000451k

The organic electrolyte of tetraethylammonium tetrafluoroborate ($TEABF_4$) in the aprotic solvent of acetonitrile (ACN) is widely used in electrochemical systems such as electrochemical capacitors. In this paper, we examine the solvation of TEA^+ and BF_4^- in ACN, and the structure, capacitance, and dynamics of the electrical double layers (EDLs) in the $TEABF_4$–ACN electrolyte using molecular dynamics simulations complemented with quantum density functional theory calculations. The solvation of TEA^+ and BF_4^- ions is found to be much weaker than that of small inorganic ions in aqueous solutions, and the ACN molecules in the solvation shell of both types of ions show only weak packing and orientational ordering. These solvation characteristics are caused by the large size, charge delocalization, and irregular shape (in the case of TEA^+ cation) of the ions. Near neutral electrodes, the double-layer structure in the organic electrolyte exhibits a rich organization: the solvent shows strong layering and orientational ordering, ions are significantly contact-adsorbed on the electrode, and alternating layers of cations/anions penetrate *ca.* 1.1 nm into the bulk electrolyte. The significant contact adsorption of ions and the alternating layering of cation/anion are new features found for EDLs in organic electrolytes. These features essentially originate from the fact that van der Waals interactions between organic ions and the electrode are strong and the partial desolvation of these ions occurs easily, as a result of the large size of the organic ions. Near charged electrodes, distinct counter-ion concentration peaks form, and the ion distribution cannot be described by the Helmholtz model or the Helmholtz + Poisson–Boltzmann model. This is because the number of counter-ions adsorbed on the electrode exceeds the number of electrons on the electrode, and the electrode is over-screened in parts of the EDL. The computed capacitances of the EDLs are in good agreement with that inferred from experimental measurements. Both the rotations (ACN only) and translations of interfacial ACN and ions are found to slow down as the electrode is electrified. We also observe an asymmetrical dependence of these motions on the sign of the electrode charge. The rotation/diffusion of ACN and the diffusion of ions in the region beyond the first ACN or ion layer differ only weakly from those in the bulk.

1. Introduction

Because of its importance in hybrid/all-electric vehicle technologies and effective use of renewable energies, electrical energy storage has gained significant attention recently.[1] Electrochemical capacitors (ECs) use the electric field of the electrical double layers (EDLs) established at the electrode/electrolyte interfaces to store energy.[2] Compared to other electrical energy storage devices such as batteries, ECs have a much higher power density and thus are ideally suited for applications that demand rapid storage and release of energy, *e.g.*, regenerative breaking.[3,4] In addition, ECs have an excellent cycle life due to the absence of the detrimental volume changes that accompany the redox reactions in batteries.[3,4] The primary limitation of ECs is their moderate energy density which is typically lower (<10 Wh kg^{-1}) than that of batteries (up to 200 Wh kg^{-1}). To address this limitation, research has been primarily focused toward developing high specific area porous electrodes.[4–6] Notably less effort has been devoted to the understanding of the EDL structures on the electrolyte side.[7] In spite of the impressive progress made recently, the gap between the energy density of ECs and other electrical energy storage devices still remains significant. To enable breakthroughs, a rational design of ECs based on both electrode material optimization and the fundamental understanding of the EDLs is necessary.

[a] *College of Engineering & Science, Clemson University, Clemson, South Carolina, 29634-0921, USA. E-mail: rqiao@clemson.edu; Web: http://www.clemson.edu/~rqiao; Fax: 864-656-4435; Tel: 864-656-5627*
[b] *Oak Ridge National Laboratory, Bethel Valley Road, Oak Ridge, Tennessee 37831-6367, USA*

† Electronic supplementary information (ESI) available: Space charge density of ACN molecules, TEA^+ cations and of BF_4^- anions; electrostatic potential distribution near a neutral electrode; concentration distribution of ACN molecules near positive electrodes; orientation of NC vector of ACN molecules with respect to the normal direction of electrodes. See DOI: 10.1039/c000451k

In this work, we focus on the EDLs at the interface of organic electrolytes and model electrodes. Organic electrolytes are widely used in ECs[8] because of their larger operating voltage (typically >2 V, as compared to *ca.* 1 V for aqueous electrolytes), which helps increase the energy density of ECs.[6] However, most work on organic electrolytes centers on the electrolytic conductivity, a stable potential window, and the dielectric constant.[9] Comparatively, atomistic level studies of such EDLs are relatively scarce.[10] The current understanding of EDLs in organic electrolytes is either inferred from capacitance measurements of carbon electrodes in organic electrolytes or is based on insight gained from the extensive studies of EDLs in aqueous electrolytes.[11] EDLs in ECs clearly involve atomistic phenomena as their thickness typically spans less than a few nanometres.

Molecular dynamics (MD) simulations of the electrode/electrolyte interface are a direct way to probe the EDLs at the molecular level, which is crucial for the understanding of charge storage mechanisms at the phase boundary. A recent study by Pratt and co-workers examined EDLs formed at the outer surface of carbon nanotubes (CNTs) immersed into organic electrolytes of 1.0 M tetraethylammonium tetrafluoroborate ($TEABF_4$) with propylene carbonate as solvent.[12] They computed the ion and electrical potential distributions near the carbon nanotube (radius = 1.17 nm) and showed that, under high electrode charge density ($|\sigma| = 0.23$ C m^{-2}), organic ions are contact-adsorbed on the CNT surfaces. Although that study revealed important aspects of the EDLs in organic electrolytes, many key questions remain unanswered: How will the structure and the capacitance of the EDLs change as the electrode charge density (or potential) changes? How will the structure and dynamics of the interfacial solvents change as the electrode becomes electrified? Will organic ions become contact-adsorbed on electrodes with small curvature or moderate charge density? What is the role of ion solvation in determining the structure of the EDLs? Can the ion distribution in EDLs be accurately described by the classical EDL models?

The objective of the present work is to investigate the structure, capacitance, and dynamics of the EDLs in an organic electrolyte using molecular dynamics (MD) simulations complemented by quantum density functional theory (DFT) calculations, with an emphasis on elucidating the above questions. We used 1.2 M $TEABF_4$ solution with acetonitrile (ACN) as a solvent because electrolytes with the same composition and similar concentration are widely used in the experimental studies of ECs.[8]

The remainder of the paper is organized as follows: section 2 presents the MD simulation system and method; section 3 presents the DFT calculations of ion solvation free energy and the MD simulations of ion solvation structure in bulk electrolytes; section 4 discusses the evolution of the EDL structure (for example, ion/solvent distribution, ion solvation, and solvent orientation) and capacitance as a function of the electrode's charge density; and section 5 presents the dynamics of ion/solvent in the EDLs with different electrode's charge densities. Finally, the conclusions are presented in section 6.

2. Simulation system and methods

Fig. 1a shows a schematic of the simulation setup. Each simulation system consists of a slab of a $TEABF_4$–ACN mixture enclosed between two electrodes. Each electrode was modeled as a static graphene layer. The separation between the geometric planes of the two electrodes was chosen as 3.9 nm. Although such a separation is much smaller than that in typical experimental studies, it is much larger than the EDL thickness near each electrode and therefore enables the EDLs at the two electrodes to be studied separately. Periodic boundary conditions were applied in the xy plane beyond the simulation box. The coordinate system was chosen such that the geometrical plane of the lower electrode corresponds to $z = 0$. The image planes of the two electrodes were placed at a position 0.08 nm from their geometrical planes (see Fig. 1a).[13] The electrical potential on the lower electrode wall was fixed to zero, and an electrical potential was ramped up from 0.0 V to 2.7 V with a 0.3 V increment and applied on the upper electrodes in separate simulations. The largest potential difference, 2.7 V, is similar to the maximum operating voltage of ECs using similar electrolytes.[8] The electrical potential on the electrode was enforced using the method developed in ref. 14. The number of ACN molecules in the system was chosen such that the ACN density at the central portion of the system did not differ by more than 5% from 14.5 M, *i.e.*, the ACN density in a 1.2 M bulk electrolyte with the same composition. The number of ions in the system was chosen such that the ion concentration in the central portion of the MD system differs less than 15% from the target concentration of 1.2 M. Additional simulations at selected potential differences in which the ion concentration at the central position of the system was varied by up to 30% indicated that the EDL structure and capacitance are insensitive to the ion concentration in the central portion of the MD system. The force fields for the electrode atoms (carbon) were taken from ref. 15. The force fields for the TEA^+ cations were taken from the General AMBER Force Field (GAFF),[16] with atomic partial charges from ref. 17. The force fields for the BF_4^- anions and ACN molecules were taken from ref. 18. The force fields for ACN molecules yield a dielectric constant of 26.3 ± 0.3 at 298 K, in reasonable agreement with the experimental value of 35.8 at room temperature.[19] Fig. 1b shows molecular models for the structure of the TEA^+ cation, the BF_4^- anion and the ACN molecule.

Simulations were performed in the NVT ensemble using a customized MD code based on Gromacs 3.2 software.[20] The system temperature was maintained at 298 K using the Berendsen thermostat with a time constant of 1.0 ps. The electrostatic interactions were computed using the PME method.[21] An FFT grid spacing of 0.11 nm and cubic interpolation for charge distribution were used to compute the electrostatic interactions in reciprocal space. A cutoff distance of 1.2 nm was used in the calculation of electrostatic interactions in real space. The non-electrostatic interactions were computed by direct summation with a cutoff length of 1.2 nm. The bond lengths of the TEA^+ and BF_4^- ions were maintained by using the LINCS algorithm,[22] while the bond angles and the dihedral angles were allowed to change.

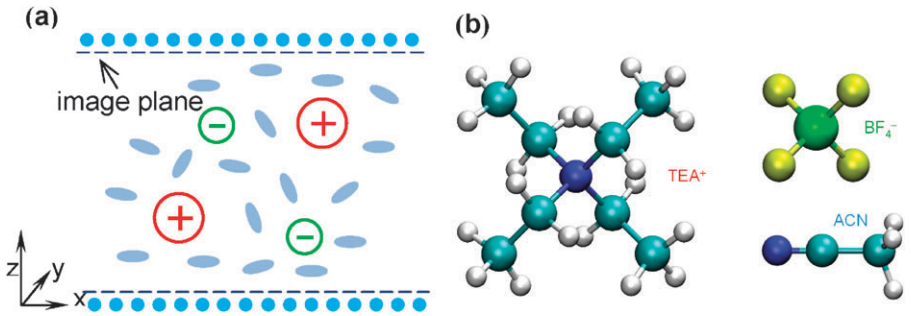

Fig. 1 (a) A schematic of the simulation system. (b) Molecular models of the TEA^+, BF_4^-, and ACN molecules.

For each applied potential on the upper electrode, five simulations with independent initial configurations were performed. In each simulation, we started the calculation at 1000 K and then annealed the system gradually to 298 K in 2 ns. Following annealing, the system was simulated at 298 K for 3 ns to reach equilibrium. Finally, a 9 ns production run was performed.

3. Ion solvation in bulk organic solvents

Ion solvation plays a key role in determining the structure of EDL in aqueous electrolytes. It affects the position of the counter-ion concentration peak near the electrodes[23] and the dynamics of interfacial ions. It is reasonable to expect that ion solvation in organic electrolytes plays a similar role. Therefore, it is useful to first quantify the solvation of TEA^+ and BF_4^- ions in bulk solutions.

3.1 Solvation free energy

Solvation free energy calculations for TEA^+ and BF_4^- in ACN were performed using the SM8 continuum solvation model[24] with the GAMESSPLUS module[25] interfaced with the GAMESS package.[26] The geometries of TEA^+ and BF_4^- in vacuum were optimized with DFT at the level of B3LYP/aug-cc-pVDZ. The geometries were then used in single point SM8 solvation calculations in conjunction with class IV CM4 charges[27] at the level of B3LYP/6-31G(d). This approach and level of theory has been shown to give accurate solvation free energies.[24] For TEA^+, we studied only two of all the possible low-energy conformations at room temperature: those with D_{2d} (global minimum) and S_4 symmetry.[28] Since experimental data on the solvation free energy of TEA^+ in ACN are not available, we performed calculations for three other cations ($EtNH_3^+$, $Et_2NH_2^+$, and Et_3NH^+) with structures similar to that of TEA^+. The solvation free energies for these cations are available from the Minnesota Solvation Database[29] and therefore the accuracy of our calculations can be verified. The optimized geometries of these three cations in vacuum are taken directly from the database.[29] As can be seen from Table 1, the computed solvation free energies of the $EtNH_3^+$, $Et_2NH_2^+$, and Et_3NH^+ cations agree very well with the experimental data in the database.[29] It is important to note that the solvation free energies tabulated in Table 1 are ΔG^*, where the asterisk denotes the Ben-Naim standard state of 24.46 atm and 298.15 K with a gas phase concentration of 1 M.[30] For the conventional standard state of 1 atm and 298.15 K, the solvation free energies ΔG° are corrected by the concentration change term of $RT\ln 24.46 = 1.89$ kcal mol^{-1}.[24,29] Thus, we obtained $\Delta G^\circ = -51.2$ and -45.1 kcal mol^{-1} for the solvation free energies of TEA^+ and BF_4^- in ACN, respectively. These values are much smaller than those of typical monovalent inorganic ions in aqueous solutions in aqueous solutions (*e.g.*, the solvation free energies of Na^+, K^+, F^-, and Cl^- ions are -98.3, -80.8, -103.8, and -75.8 kcal mol^{-1}, respectively[31]).

3.2 Solvation structure

Explicit ion solvation is first quantified by the density distribution of ACN molecules around the ions. Fig. 2a shows the ion–ACN and ion–ion radial distribution functions (RDFs) in a bulk solution of 1.2 M $TEABF_4$ in ACN. The TEA^+–ACN RDF indicates that the first peak is rather broad and the second peak is barely distinguishable from the first. This suggests that the solvation of TEA^+ cations by ACN molecules lacks a distinct structure of solvation shells compared to that observed for solvation of small inorganic ions in aqueous solutions.[32] The low value and broadness of the first peak is caused by (1) the large size of the TEA^+ cations, which leads to weak electrostatic ion–ACN interaction, (2) the charge de-localization (*i.e.*, the net charge of a TEA^+ cation is distributed among its multiple atoms) that weakens the electrostatic attraction between the ion and the ACN molecules near it, and (3) the irregular shape of the TEA^+ cations that prevents a dense packing of ACN molecules around them with a uniform distance to the center of TEA^+. The RDF for BF_4^-–ACN shows similar features, although the first peak becomes more distinct because of the

Table 1 Solvation free energies for several ions in ACN calculated using the SM8 solvation model and compared with experimental values from the literature

Ions	Symmetry	$\Delta G^*(sol)^{a,b}$/kcal mol^{-1}		Error/kcal mol^{-1}
		SM8[b]	Reference[c]	
$EtNH_3^+$	C_s	−80.4	−76.8	−3.6
$Et_2NH_2^+$	C_{2v}	−68.3	−67.5	−0.8
Et_3NH^+	C_3	−59.0	−59.8	0.8
TEA^+	D_{2d}	−53.1	—	—
	S_4	−53.1	—	—
BF_4^-	T_d	−47.0	—	—

[a] The asterisk denotes the Ben-Naim standard state of 24.4 atm and 298.15 K.[30] Such a state gives a gas phase concentration of 1 M, the same as that in the solution phase. [b] Calculated using the SM8 model coupled with class IV CM4 charges at the level of B3LYP/6-31G(d). [c] Reference values from the Minnesota Solvation Database (ref. 29).

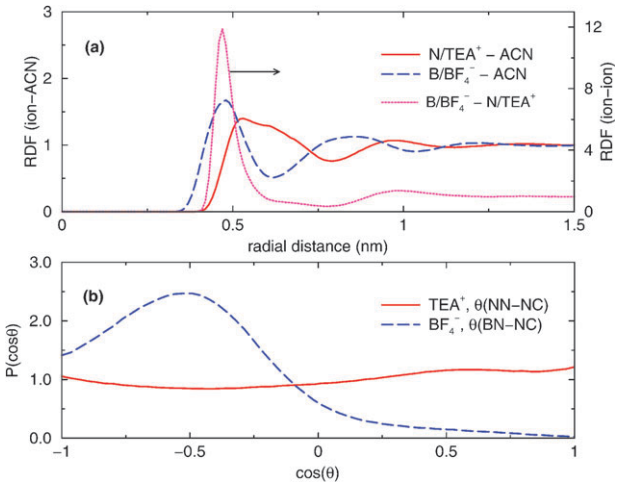

Fig. 2 (a) Ion–ACN and ion–ion radial distribution functions (RDF) in 1.2 M bulk $TEABF_4$–ACN solution. The radial distance is between the ion center, either N or B, and the center of mass of ACN molecules. (b) Distribution of the angle θ formed between the NC vector of the ACN molecules in the first solvation shell of TEA^+ and BF_4^- ions and the vector from the ion center, either N or B, to the N atom of the ACN molecules.

smaller size and more spherical shape of the BF_4^- anions. The RDF radius of *ca.* 0.5 nm for the first solvation shell of BF_4^- anion indicates that the solvated ion diameter of BF_4^- is *ca.* 1 nm. When compared to the bare ion diameter of BF_4^- (4.6 Å),[33] this solvated ion diameter yields a solvation shell thickness of *ca.* 0.5 nm, which is comparable to the dimension of one shell of ACN molecules according to a radial distribution of solvent molecules (see below). In addition, the solvated ion diameter of 1 nm is in good agreement with the pore width of $\leq$1 nm necessary for the desolvation of BF_4^- anions in ACN according to the anomalous increase in capacitance in microporous carbons.[34] The solvation numbers of the TEA^+ and BF_4^- ions, defined as the number of ACN molecules within the first solvation shell of the ions, were found to be 15.5 and 6.75, respectively. We note that, following traditional conventions, the extension of the first solvation shell is determined by the position of the first local minimum of the ion–ACN RDFs shown in Fig. 2a.

Fig. 2a also shows the RDF for the TEA^+–BF_4^- ion pair, which has essentially one main peak located at 0.47 nm. On the basis of the bare ion diameter of TEA^+ (6.8 Å) and BF_4^- (4.6 Å)[33] and the first peak location of the BF_4^-–ACN and TEA^+–ACN RDF curves, we can infer that TEA^+ and BF_4^- ions constitute a so-called "contact ion pair" in the solution. This is not surprising since the solvent does not effectively screen the electrostatic attraction due to the relatively small dielectric constant of ACN. The high RDF peak suggests that the correlation between TEA^+ and BF_4^- ions is strong in ACN solutions. This correlation should affect the ion distribution inside the EDLs.[35]

The ion solvation is further quantified in Fig. 2b by examining the orientational ordering of the ACN molecules in the first solvation shell of the TEA^+ and BF_4^- ions. We computed the distribution of the angle θ formed between the NC vector of ACN molecules within an ion's first solvation shell and the vector from the ion center, either N or B, to the N atom of the ACN molecules. The NC vector points from the N atom to the methyl group's C atom. Fig. 2b shows that ACN molecules are nearly randomly oriented in the first solvation shell of TEA^+ cation, which is in sharp contrast with the strongly oriented water molecules near small inorganic ions.[32] The weak orientational ordering of ACN molecules around the TEA^+ cation originates from the large size and irregular shape of the TEA^+ cations. Fig. 2b shows that the orientational ordering of ACN near BF_4^- anions, although still weaker than those of the water molecules near small inorganic ions, is stronger than that near the TEA^+ cations. Specifically, ACN molecules tend to align their NC vectors away from the BF_4^- anion at an angle of 60°. The average NC vector orientation angle cos θ was found to be −0.51, which is close to that observed for ACN molecules near model anions with a net charge of −0.75 e and van der Waals diameter of 0.31 nm.[36]

In summary, the above results show that the solvation of TEA^+ and BF_4^- ions in ACN is characterized by the weak packing/orientational ordering of ACN molecules around the ions and a moderate solvation free energy. The solvation of both ions in ACN is much weaker compared to the solvation of small inorganic ions in aqueous solution. Hence it is possible that organic ions can become partially desolvated at much weaker electrode polarization compared to that in aqueous electrolytes.

4. Structure and capacitance of EDLs

4.1 EDLs near electrodes at potential of zero charge

Understanding the structure of the EDLs near electrodes at potential of zero charge (PZC) provides a baseline for describing EDLs near polarized electrodes. In addition, the insight gained from studying such EDLs facilitates the understanding of EDLs near weakly polarized electrodes, which is important in applications such as electrochemical sensing. Fig. 3a shows the concentration distribution of ACN molecules near the electrode. We note that throughout this paper, the positions of solvent molecules and ions are based on their center of mass. A significant layering of ACN molecules is observed near the electrode. The first layer of ACN molecules is found to occupy the region z = 0 to 0.56 nm (zone 1 in Fig. 3a), and additional layers of ACN molecules are observed in region z = 0.56 to 1.1 nm (zone 2). At positions beyond about 1.1 nm from the electrode, the structure of ACN becomes bulk-like. The rich structure of ACN observed is caused mainly by the short-range solvent–solvent and solvent–electrode interactions and resembles the water structure near solid surfaces reported in numerous studies.[23,37]

Fig. 3b shows the distribution of the angle formed between the NC vectors of ACN molecules and the normal direction of the electrode for ACN molecules at different distances from the electrode. We observe that a majority of ACN molecules in the first ACN layer (zone 1) orient with their molecular axis parallel to the electrode surface. Since quantum mechanical processes such as bonding between ACN molecules and electrode atoms are not taken into account in our classical

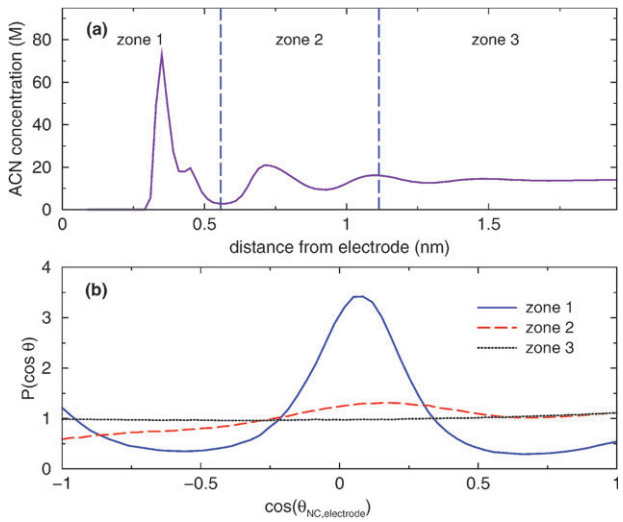

Fig. 3 (a) Concentration distribution of ACN molecules near a neutral electrode. The position of ACN molecules is based on their center-of-mass. (b) Orientational distribution of the NC vector of ACN molecules (defined as the vector pointing from the N atom of an ACN molecule to the C atom of its methyl group) with respect to the normal direction of the electrode for ACN molecules at different distances from the electrode.

MD simulations, such an orientation is adopted by the ACN molecules mainly to maximize their van der Waals interactions with the electrode. This preferential orientation is similar to the side-on adsorption mode of ACN molecules on an uncharged Pt surface, which are energetically more favorable than the end-on adsorption modes with the CN group pointing towards or away from the Pt surface.[38] Our results also complement the experimental findings inferred from the sum frequency generation (SFG) measurements of ACN orientation on Pt(111) surface.[39] In the experimental study, it was found that ACN molecules adopt an orientation with the CN group directed towards or away from the surface when the surface is positively or negatively charged, respectively. In comparison, ACN molecules do not have such preferred orientations at PZC,[39] and our simulations indicate that there is a preference for side-on orientations under this condition. Fig. 3b also shows that the orientational ordering of ACN molecules is already weak beyond the first ACN layer. At a distance of 1.1 nm beyond the electrode, the ACN orientation approaches a random distribution. The penetration of ACN orientational ordering into the bulk electrolyte is *ca.* 0.3–0.6 nm shorter compared to that for ACN molecules near TiO_2 anatase (101) surfaces.[40] The shallower penetration in our system originates mainly from the weaker interactions between ACN molecules and the electrode atoms, which induce weaker ACN orientational ordering in the first ACN layer and thus weaker orientational ordering beyond the first ACN layer.

Fig. 4b shows the concentration distribution of TEA^+ and BF_4^- ions near a neutral electrode, and the circles indicate the size of bare TEA^+ and BF_4^- ions (0.68 nm and 0.46 nm, respectively[33]). For reference, the ACN concentration profile is shown in Fig. 4a. As indicated by the twin-peaks located at z = 0.48 and 0.52 nm for the TEA^+ cation and the peak located at z = 0.46 nm for the BF_4^- anions, a large amount of TEA^+ and BF_4^- ions are adsorbed on the electrode. Based on the size of bare TEA^+ and BF_4^- ions (*cf.* the two circles in Fig. 4b) and the ACN concentration profile shown in Fig. 4a, there are no ACN molecules between ions located in these peaks and the electrode, *i.e.*, these ions are contact-adsorbed on the electrode. This suggests that, even at zero electrode charge density, some ions can be adsorbed on the electrode and become partly desolvated. This phenomenon is similar to the adsorption of I^- and Cl^- ions onto a neutral electrode as observed in aqueous solutions.[41] The significant contact adsorption of the organic ions is due to several different factors.[41] First, the solvation free energies of these ions are not as high as those of the small inorganic ions, and thus it is easier for the ions to lose part of their solvation shell and become contact-adsorbed. Second, because of the large size of these ions, they will not lose a large fraction of their solvation shell, even upon contact adsorption. The TEA^+ and BF_4^- ions in the first peak near the electrode are found to lose *ca.* 30% and *ca.* 40% of their solvation shell, respectively. Finally, because of the large ion size and large number of atoms in each ion, the non-electrostatic ion–electrode interactions (essentially the van der Waals attractions) are strong, which facilitates the adsorption of ions on the electrode. Typical examples of the ubiquitous van der Waals forces are seen in nano-confined systems, such as the encapsulation of organic molecules in carbon nanotubes.[42] Fig. 5 shows the potential energies of the TEA^+ and BF_4^- ions at different positions above a neutral electrode due to such interactions. The valleys of these potential profiles are deep (−89.3 and −17.8 kJ mol^{-1} for the TEA^+ and BF_4^- ions, respectively). For TEA^+ cation, the valley of the potential energy profile even becomes comparable to the ion's solvation free energy, which means that the energy cost for the desolvation can be compensated by the non-electrostatic ion–electrode interaction. In most double layer theories, the non-electrostatic ion–electrode interactions are neglected. However, the above results suggest that, for bulky ions, such interactions are major driving forces for the partial desolvation of ions as they move toward the electrode, and must be considered in order to accurately predict the ion adsorption on the electrode. Fig. 4b also shows that TEA^+ and BF_4^- ions form alternating layers near the electrode, which is not typically observed in aqueous media but is prevalent in room-temperature ionic liquids.[37,43] The alternating layers of cations and anions are caused by the strong correlation between these ions, as is evident in Fig. 2a. Fig. 4c summarizes the arrangement of ACN molecules, TEA^+, and BF_4^- ions near a neutral electrode.

Charge separation and electrical potential distribution of the above EDLs were also studied. Details are given in the ESI.† We found that there exists a small potential difference of 0.168 V between the electrode and the bulk electrolyte even though the electrodes are not electrified, as a result of the preferential orientation of the ACN molecules. This small potential difference represents the potential of zero charge (PZC) of the electrode/electrolyte system studied here.

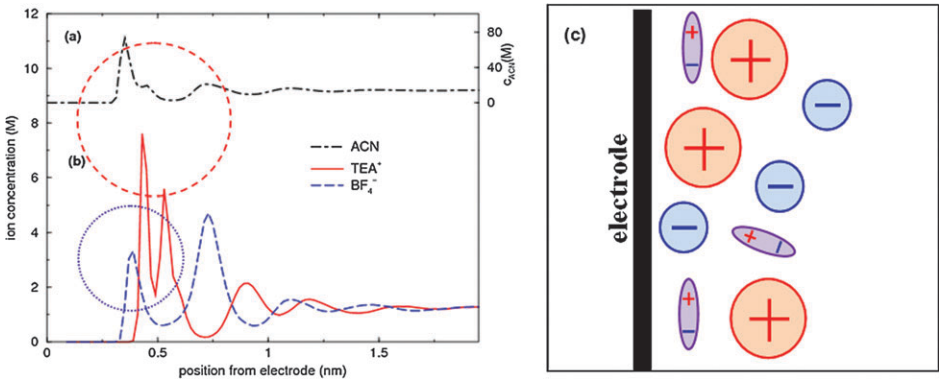

Fig. 4 (a) and (b) Concentration distributions of ACN, TEA^+ and BF_4^- near a neutral electrode. Circles are bare ion diameters of the TEA^+ and BF_4^- ions. (c) Schematic of the arrangement of ACN molecules, TEA^+ and BF_4^- ions near a neutral electrode. The ellipses denote ACN molecules.

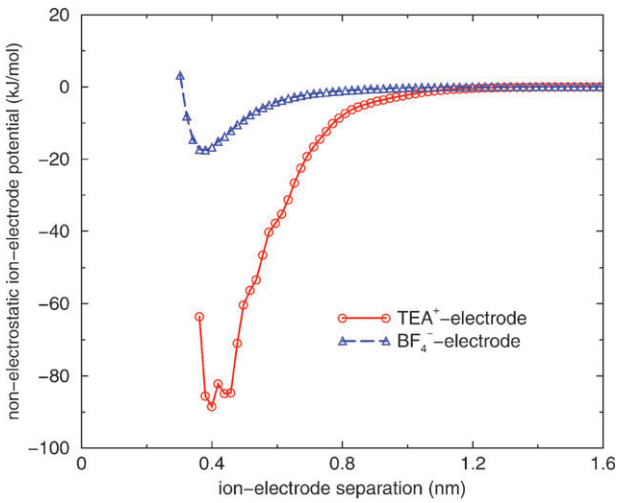

Fig. 5 Potential energy of the TEA^+ cation and BF_4^- anion at different positions above a neutral electrode due to non-electrostatic ion–electrode interactions.

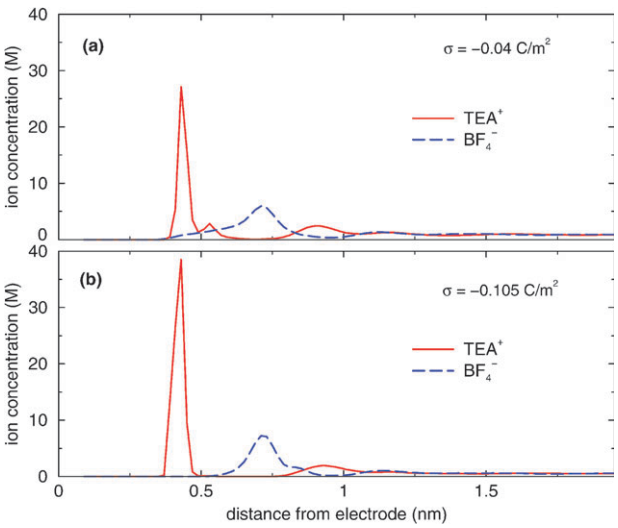

Fig. 6 Concentration profiles of TEA^+ cations and BF_4^- anions near electrodes with charge densities of -0.04 C m^{-2} (panel a) and -0.105 C m^{-2} (panel b).

4.2 Structure of EDLs near negative electrodes

As the potential difference between the upper and lower electrodes increases, the electrode surface charge density σ increases. Here we focus on the EDLs adjacent to the lower electrode at a potential difference of 0.9 V and 2.7 V, when the surface charge density on the lower electrode is -0.04 C m^{-2} and -0.105 C m^{-2}, respectively. Fig. 6a and b show the concentration profiles of the TEA^+ cations and BF_4^- anions near the negative electrode at $\sigma = -0.04$ and -0.105 C m^{-2}, respectively. We observe that, as σ increases, more TEA^+ cations become contact-adsorbed, and the first TEA^+ concentration peak moves slightly towards the electrode. The accumulation of TEA^+ cations near the electrode is accompanied by the depletion of BF_4^- anions in the same region: contact adsorption of BF_4^- becomes minor at $\sigma = -0.04$ C m^{-2} and vanishes at $\sigma = -0.105$ C m^{-2}. However, a large number of BF_4^- anions accumulate at a position 0.72 nm from the electrode, and this BF_4^- peak is followed by a weak TEA^+ peak located at $z = 0.92$ nm. The alternating counter-ion/co-ion peaks are again caused by the strong association of BF_4^- and TEA^+ ions as shown in Fig. 2a. The TEA^+ and BF_4^- ion concentrations become the same only when $z > 1.1$ nm.

The ion distributions shown in Fig. 6 cannot be adequately described by the current classical EDL models. Even though the Helmholtz model predicts distinct counter-ion concentration peaks near the electrode similar to those found here, the Helmholtz model also indicates that the ion concentration becomes homogeneous beyond the first counter-ion peak, which contradicts the alternating counter-ion/co-ion peaks shown in Fig. 6. In addition, the Helmholtz model specifies that the charge of the counter-ions within the Helmholtz plane exactly balances the net charge of the electrode, in sharp contrast to what we have found. To show this, we computed the "effective ion accumulation" (EIA) factor

$$EIA(z) = L_x L_y \int_0^z [\rho^n_{\text{counter-ion}}(s) - \rho^n_{\text{co-ion}}(s)]\mathrm{d}s, \qquad (1)$$

where z and s are the distance from the electrode, L_x and L_y are the size of the simulation box in the x- and y-directions, $\rho^n_{\text{counter-ion}}$ and $\rho^n_{\text{co-ion}}$ are the number density of the counter-ion and the co-ion. $EIA(z)$ indicates the difference between the number of counter-ions and co-ions in the space within position z from the electrode. The Helmholtz model predicts that $EIA(z)$ reaches the number corresponding to the net

charge (in unit of elementary charge) on the electrode at the Helmholtz plane and shows no change at other positions. The trend of $EIA(z)$ is the same near electrodes with $\sigma = -0.04$ and -0.105 C m^{-2}, and we show only $EIA(z)$ near the electrode with $\sigma = -0.105$ C m^{-2} in Fig. 7a. We observe that, at $z = 0.49$ nm (the right edge of the first TEA^+ concentration peak, see Fig. 6b), EIA reaches 9.46, which is 1.64 times the total number of electrons on the electrode. Since the BF_4^- anion concentration is zero for $z < 0.5$ nm, we conclude that the number of TEA^+ cations adsorbed on the electrode exceeds the total number of electrons on the electrode, in qualitative disagreement with the Helmholtz model. The above $EIA(z)$ profile indicates that the electrode may be over-screened at $z = 0.49$ nm, but the delocalized nature of charge on the ions prevents a quantitative conclusion to be drawn. To better quantify the charge screening, we introduce a charge screening factor

$$C_f(z) = \int_0^z [\rho^e_{\text{co-ion}}(s) - \rho^e_{\text{counter-ion}}(s)]ds/\sigma, \qquad (2)$$

where $\rho^e_{\text{counter-ion}}$ and $\rho^e_{\text{co-ion}}$ are the space charge density of the counter-ion and the co-ion, respectively. $C_f(z) = 1.0$ corresponds to a complete screening of the electrode charge at position z, and $C_f(z) > 1.0$ corresponds to an over-screening of the electrode charge. The Helmholtz model predicts that $C_f(z)$ reaches 1.0 at the Helmholtz plane and remains 1.0 at positions beyond that. The more sophisticated Poisson–Boltzmann (PB) or Stern/Helmholtz + PB models predict that $C_f(z)$ reaches 1.0 at several Debye lengths from the electrode but never exceeds 1.0. Fig. 7b shows that the variation of $C_f(z)$ near the electrode with $\sigma = -0.105$ C m^{-2}. $C_f(z)$ is larger than 1.0 in the region 0.5 nm $< z <$ 0.86 nm. This is not entirely surprising since strong correlation between the counter-ion and co-ions, which is not accounted for in the classical PB model, is known to cause over-screening of the electrode (often termed "charge inversion").[35]

The dense packing of TEA^+ cations near the electrode can potentially lead to changes in the solvation of the interfacial

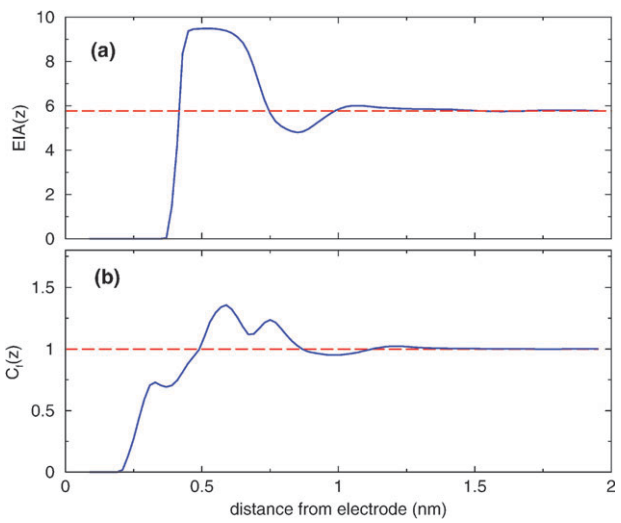

Fig. 7 Variation of the effective ion accumulation (EIA) factor (panel a) and the charge screening factor (C_f) (panel b) near an electrode with $\sigma = -0.105$ C m^{-2}. See text for definition of EIA and C_f factors.

ions, *i.e.*, some TEA^+ cations might lose more of their solvation shell due to their small separation with other TEA^+ cations adsorbed on the electrode. To determine to what extent the contact adsorbed TEA^+ cations lose their solvation shell in the direction parallel to the electrode, we computed the average distance between the contact-adsorbed TEA^+ cations by assuming that these ions are packed hexagonally on the electrode. The average distance between these TEA^+ cations was found to be 1.32 nm and 1.04 nm for $\sigma = -0.04$ and -0.105 C m^{-2}, respectively. Since these separations are smaller than the diameter of solvated TEA^+ cations (1.58 nm, see Fig. 2a), we conclude that, for the electrode charge densities studied, TEA^+ cations contact-adsorbed on the electrode shed part of their solvation shell. This is not only due to the geometrical confinement by the electrode, but also due to the lateral confinement by other TEA^+ cations. In particular, at $\sigma = -0.105$ C m^{-2}, there are few ACN molecules between the TEA^+ cations adsorbed on the electrode.

The adsorption of counter-ions on the electrode also changes the structure of interfacial solvents. Fig. 8a shows the concentration profiles of ACN molecules near the electrodes with $\sigma = 0$, -0.04, and -0.105 C m^{-2}. The first ACN peak decreases significantly as the electrode charge density increases. This is caused by displacement of ACN molecules by the bulky TEA^+ cations adsorbed on the electrode. Note that the sharp ACN concentration peak at $\sigma = 0$ and -0.04 C m^{-2} is broadened and has a much lower peak when σ increases to -0.105 C m^{-2}. This is partly due to the large change in ACN orientation. Fig. 8b shows the orientation of the NC vector of ACN molecules within 0.56 nm from the electrode with respect to the normal direction of the electrode, at different electrode charge densities. We observe that, as σ becomes more negative, the ACN molecules orient their methyl group closer to the electrode than their nitrogen atom. At $\sigma = -0.105$ C m^{-2}, *ca.* 50% of the ACN molecules in the first ACN layer are oriented with their NC vector pointing at an angle equal to or larger than 120° with respect to the normal direction of the electrode, consistent with that inferred from the SFG measurements.[39] Compared to the situations at $\sigma = 0$ or $\sigma = -0.04$ C m^{-2}, such an orientation of the ACN molecules reduces the overall non-electrostatic attraction exerted on the ACN molecules by the electrode, and leads to a less sharp but wider span of the first ACN peak compared to those when $\sigma = 0$ and -0.04 C m^{-2}. The orientational ordering of the NC vectors of ACN molecules becomes weak for $z > 0.56$ nm and thus are not shown.

4.3 Structure of EDLs near positive electrodes

Fig. 9a and b show the concentration distribution of TEA^+ and BF_4^- ions near electrodes with $\sigma = +0.04$ and $+0.105$ C m^{-2}. The trends of the counter-ion and co-ion distribution, such as significant contact adsorption of the counter-ion on the electrode, alternating counter-ion/co-ion concentration peaks, and over-screening of the electrode charge, are similar to those observed near the negative electrode. The primary difference between the EDL structures near the positive and negative electrodes lies in the solvation of the counter-ions

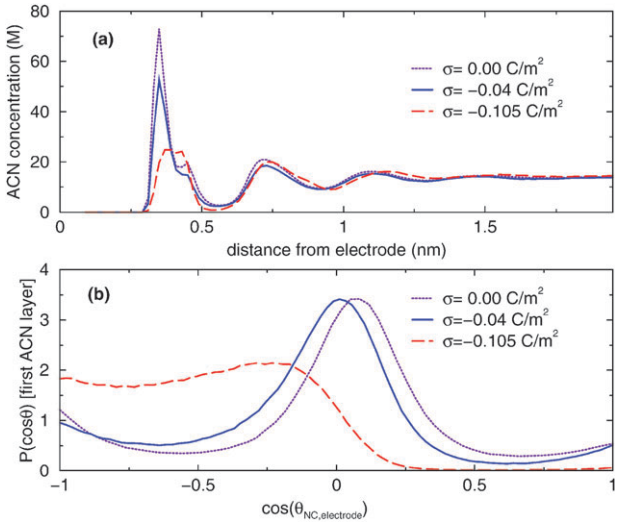

Fig. 8 (a) Concentration distribution of ACN molecules near electrodes with various charge densities. (b) Orientation distribution of the NC vector (defined in the caption of Fig. 3) of ACN molecules within 0.56 nm of the electrode with respect to the normal direction of electrodes.

contact-adsorbed on the electrodes. The average lateral spacing between the BF_4^- anions adsorbed on electrodes with $\sigma = +0.04$ and $+0.105$ C m^{-2} was found to be 1.43 nm and 0.98 nm, respectively. Since the diameter of a solvated BF_4^- anion in the bulk is 1.2 nm (Fig. 2a), we conclude that, the solvation of contact adsorbed BF_4^- anions is hardly perturbed by their neighbors near electrodes with $\sigma = +0.040$ C m^{-2}, but becomes moderately perturbed when $\sigma = +0.105$ C m^{-2}. The evolution of the ACN concentration profile near the electrode as the magnitude of electrode charge density increases is similar to that observed near the negative electrode and will not be discussed further. As expected,[39] when the electrode charge density becomes more positive, the NC vectors of the interfacial ACN molecules become more aligned with the normal direction of the electrode. The results are deposited in the ESI† for brevity.

4.4 EDL capacitance

Since the electrical potential in the central portion of the MD system is constant, the potential drop across the EDLs near each of the electrodes, ϕ_{EDL}, can be computed separately. We computed ϕ_{EDL} for EDLs near the positive and negative electrodes as the potential differences between the two electrodes increases from 0 to 2.7 V (Fig. 10a). To compute the capacitance C_{edl} of the EDLs, we first fitted the ϕ_{EDL}–σ correlation to a fourth-order polynomial and then computed C_{edl} by

$$C_{edl}(\sigma) = \frac{\sigma}{\phi_{EDL}(\sigma) - PZC}. \quad (3)$$

In the literature, C_{edl} is often computed by $C_{edl} = \sigma/\phi_{EDL}$, which is a good approximation to the exact definition given by eqn (3) only when $\phi_{EDL} \gg PZC$. In the present study, ϕ_{EDL} is less than 1.5 V and PZC = 0.168 V, hence it is necessary to use eqn (3) to accurately compute C_{edl}. Fig. 10b shows C_{edl} as a function of the electrode charge density and the magnitude of the capacitance is similar to that found in experiments, *e.g.*, the capacitance of planar carbon electrode immersed in a $TEABF_4$–ACN electrolyte extrapolated from capacitance of carbon mesoporous pores is 0.09 F m^{-2}.[44] We observe that C_{edl} is relatively insensitive to the electrode charge density—C_{edl} remains nearly a constant between $\sigma = 0$ to $+0.105$ C m^{-2} and C_{edl} for EDLs near negative electrodes decreases moderately (*ca.* 27%) as σ increases from 0 to -0.105 C m^{-2}. The weak dependence of C_{edl} is consistent with the experimental observation in the galvanostatic charge/discharge, where the slope of cell voltage *versus* time is nearly independent of voltage window.[34b] Near electrodes with $|\sigma| = +0.105$ C m^{-2}, C_{edl} is 27% higher when the BF_4^- anions are the counter-ions compared to when TEA^+ cations are the counter-ions. This is due to the smaller size of the BF_4^-

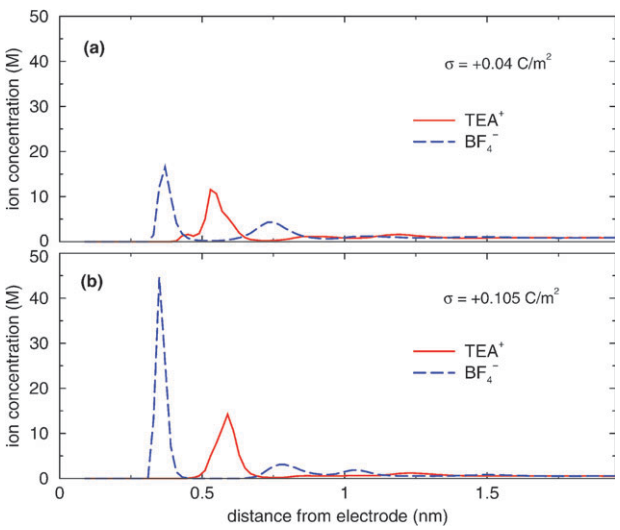

Fig. 9 Concentration distribution of TEA^+ and BF_4^- ions near electrodes with charge densities of $+0.04$ C m^{-2} (panel a) and $+0.105$ C m^{-2} (panel b).

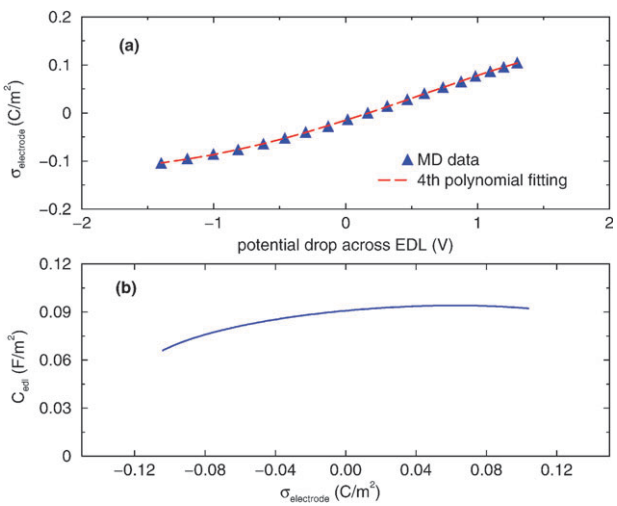

Fig. 10 (a) Relation between electrode charge density and potential drop across the EDLs adjacent to the electrodes. (b) Capacitance C_{edl} of the EDLs adjacent to the electrodes with different surface charge densities.

anions compared to that of the TEA^+ cations, which allows them to approach closer to the electrode.

The good agreement between the capacitance predicted by MD simulations and that inferred from experimental studies suggests that the key aspects of the EDLs are captured. However, we note that many aspects of the EDLs have yet to be incorporated with sufficient detail. Most importantly, the electronic degrees of freedom of the electrode have largely been neglected in the existing literature. In our simulations, the electrode is modeled as an object of uniform potential and the electrostatic interactions between the electrode and charges inside the system are treated classically. In addition, the quantum nature of the electrode is only considered *via* the concept of electrode image plane, positioned 0.08 nm away from the electrode. However, the effective location of the image plane of an electrode is known to shift as its surface charge density changes.[45] Therefore, the dependence of the capacitance on the electrode charge density should be taken as semi-quantitative. A more accurate modeling of the EDLs and calculation of the capacitance should take into account the coupling between the electronic degrees of freedom of the electrode and the solvent/ion structure on the electrolyte side. Simulations of this type have been attempted for EDLs in aqueous electrolyte[46] but have not been reported for EDLs in organic electrolytes.

5. Dynamics of EDLs

5.1 Solvent rotational dynamics

The electrochemical decomposition of organic solvents is closely related to the translational and rotational dynamics of the interfacial solvents. Here we first quantify the rotational dynamics of ACN molecules by computing the dipole auto-correlation function d_{ACF}

$$d_{ACF}(t) = \langle \boldsymbol{p}_i(0)\cdot\boldsymbol{p}_i(t)\rangle / \langle \boldsymbol{p}_i(0)\cdot\boldsymbol{p}_i(0)\rangle \quad (4)$$

where $\boldsymbol{p}_i$ is the dipole moment of an ACN molecule i. A faster decay of $d_{ACF}(t)$ corresponds to a freer rotation of the molecule. Fig. 11a shows $d_{ACF}(t)$ for the ACN molecules in the regions of $z < 0.56$ nm (*i.e.*, the first ACN layer). We observe that the rotation of the ACN molecules in the first ACN layer is significantly retarded compared to that in the bulk, even at zero electrode charge density. As the electrode becomes electrified, the rotation of these ACN molecules, are generally more hindered. For the same magnitude of electrode charge density, the rotation has an asymmetric dependence on the sign of the electrode charge. Interfacial ACN molecules rotate more freely near electrodes with $\sigma = +0.04$ C m^{-2} than that near electrodes with $\sigma = -0.04$ C m^{-2}, and the opposite trend is observed when $|\sigma| = 0.105$ C m^{-2}. To understand these observations, we note that compared to that of the ACN molecules in bulk, the rotation of interfacial ACN molecules is retarded by additional mechanisms: (1) hindrance by the electrode, and (2) interference by the ions adsorbed on the electrode. As the electrode becomes electrified, hindrance of ACN rotation by the electrode and by the ions adsorbed on the electrodes increases simultaneously since the ACN–electrode interactions become stronger and more counter-ions are adsorbed on the electrode. Consequently the quasi-free rotation of ACN molecules decreases. At $|\sigma| = 0.04$ C m^{-2}, the average distance between the TEA^+ cations adsorbed on the negative electrode (1.32 nm) is smaller than that between the BF_4^- anions adsorbed on the positive electrode (1.43 nm). This fact, along with the larger size of the TEA^+ cations, indicates that the interfacial ACN molecules occupying the space between TEA^+ cations adsorbed on negative electrodes are more confined in the lateral direction. Hence their rotation is more difficult than that of the ACN molecules adjacent to positive electrodes. At $|\sigma| = 0.105$ C m^{-2}, the geometrical confinement created by the TEA^+ cations adsorbed on the negative electrode is still stronger compared to that of BF_4^- anions adsorbed on the positive electrode. However, since the ACN–BF_4^- interactions are stronger than the ACN–TEA^+ interactions (see Fig. 2), the rotation of ACN molecules adjacent to the positive electrodes slows down slightly more than those adjacent to the negative electrodes.

Fig. 11b shows $d_{ACF}(t)$ for the ACN molecules in region 0.56 nm $< z < 1.12$ nm. The decay of these dipole auto-correlation functions is similar to that in the bulk and is not strongly affected by the electrification of the electrodes. This shows that the influence of the electrode on the ACN rotation dynamics is limited primarily to the first ACN layers adjacent to the electrode. This is consistent with the observation that ACN structure (*e.g.*, concentration and orientation) becomes nearly homogeneous beyond the first ACN layer adjacent to the electrode.

5.2 Solvent and ion diffusion

The self diffusion coefficients of TEA^+, BF_4^- and ACN molecules in our MD system were determined by integrating their velocity autocorrelation functions. We found that the diffusion coefficients deviate from bulk values primarily in the region within 0.56 nm from the electrode. Therefore, only the diffusion coefficients in this region are shown in Table 2. For the ACN molecules adjacent to their electrodes, their diffusion shows several features: (1) it is strongly anisotropic: near the same electrode, the diffusion coefficients in directions parallel to the electrode ($D_{//}$) are *ca.* 2.6–2.9 times larger than those in the direction normal to the electrode ($D_\perp$), (2) $D_{//}$ near the electrodes is always smaller than that in the bulk and decreases moderately as the electrodes become electrified, (3) there is an asymmetry in the dependence of $D_{//}$ on the sign of electrode charge. Similar asymmetry can also be observed for $D_\perp$, but it is much weaker. Observation 1 can be rationalized by the geometrical confinement imposed on the ACN molecule by the electrode, and similar anisotropy has long been observed for other interfacial fluids.[47] Observation 2 is related to the fact that as the electrodes are electrified, they interact stronger with the ACN molecules and more counter-ions become contact-adsorbed on the electrodes, both of which restrict the diffusion of ACN molecules. Observation 3 has the same origin with the asymmetric dependence of rotational motion on the sign of electrode charge as discussed in section 5.1. Specifically, at $|\sigma| = 0.04$ C m^{-2}, the slower diffusion of ACN molecules near electrode with $\sigma = -0.04$ C m^{-2} is due to the weaker lateral confinement imposed by the TEA^+ cations adsorbed on the

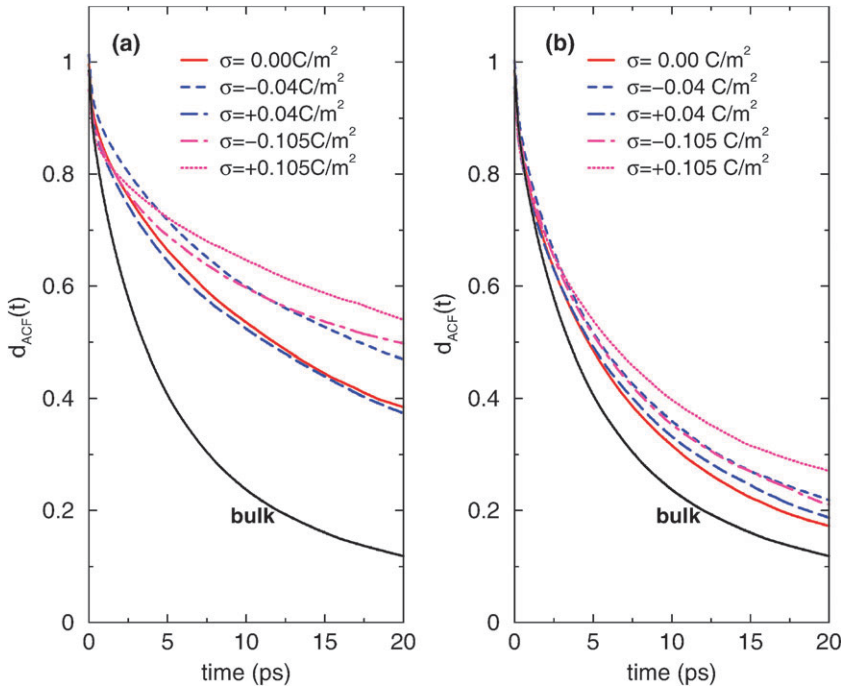

Fig. 11 Dipole autocorrelation function for ACN molecules at different locations from the electrodes. (a) ACN molecules in region $z < 0.56$ nm; (b) ACN molecules in region 0.56 nm $< z <$ 1.12 nm.

electrode. At $|\sigma| = 0.105$ C m^{-2}, the slower diffusion of ACN molecules near electrodes with $\sigma = +0.105$ C m^{-2} is due to their stronger interactions with the BF_4^- anions adsorbed on the positive electrode. As these mechanisms primarily constrain the motion of ACN molecules in the direction parallel to the electrode, the asymmetrical dependence of $D_\perp$ on the sign of electrode charge is much weaker.

The diffusion of TEA^+ and BF_4^- ions shows similar features to those of the ACN molecules, *e.g.*, anisotropy and decrease of $D_\perp$ as the electrode charge density increases. An interesting difference is that, $D_{//}$ of interfacial ions is only weakly affected by the electrode. For TEA^+ cations, $D_{//}$ near all electrodes is only slightly smaller than that in the bulk, and their dependence on the electrode charge is negligible. For BF_4^- anions, $D_{//}$ near electrodes with $\sigma = 0$ and $+0.04$ C m^{-2} are even larger than that in the bulk. To understand these phenomena, we note that TEA^+ and BF_4^- ions form contact ion pairs in bulk electrolytes, which significantly deteriorate their diffusion. When these ions are adsorbed on the electrodes, the number of ion pairs that they participate in is reduced by the electrode and thus, their diffusion is much less constrained. While the ion diffusion in directions parallel to the electrode is made more difficult by the electrode–ion interactions, this effect is less important because of the atomically smooth electrodes used in this study. Therefore, the lateral diffusion of ions near moderately charged electrodes is comparable to, or faster than, that in the bulk. In addition to the above mechanism, the diffusion of interfacial ions is also hindered by other interfacial ions. The diffusion coefficient of interfacial ions is a result of the competition between these mechanisms. The results collated in Table 2 show that, for larger TEA^+ cations or BF_4^- anions near highly charged electrodes, the latter mechanism dominates; for smaller BF_4^- anions near neutral or moderately charged electrode, the first mechanism dominates.

6. Conclusions

The solvation of TEA^+ and BF_4^- ions in bulk ACN was studied using MD simulations complemented with quantum DFT calculations. The solvation free energies of TEA^+ and BF_4^- ions were found to be -51 kcal mol^{-1} and -45 kcal mol^{-1}, respectively, which are much smaller than those of typical small

Table 2 Self diffusion coefficients of molecules (in unit of 10^{-9} m^2 s^{-1}) in the region of 0.56 nm from the electrode[a]

	ACN		TEA^+		BF_4^-	
$\sigma_{electrode}$/C m^{-2}	$D_{//}$	$D_\perp$	$D_{//}$	$D_\perp$	$D_{//}$	$D_\perp$
0	1.92 ± 0.18	0.68 ± 0.06	0.87 ± 0.13	0.15 ± 0.02	1.00 ± 0.13	0.17 ± 0.03
−0.04	1.66 ± 0.10	0.63 ± 0.03	0.79 ± 0.11	0.13 ± 0.02	×	×
+0.04	1.90 ± 0.13	0.65 ± 0.07	×	×	0.89 ± 0.05	0.23 ± 0.04
−0.105	1.53 ± 0.04	0.52 ± 0.02	0.80 ± 0.08	0.09 ± 0.03	×	×
+0.105	1.25 ± 0.10	0.46 ± 0.07	×	×	0.74 ± 0.09	0.19 ± 0.01
In bulk	2.34 ± 0.06		0.96 ± 0.02		0.82 ± 0.05	

[a] Symbol × indicates that $D_{//}$ and $D_\perp$ cannot be accurately computed due to the scarcity of molecules in the region.

inorganic ions in aqueous solutions. The ACN molecules in the solvation shell of both ions show only weak packing and orientational ordering, which are caused by the large size, charge delocalization, and irregular shape (in the case of TEA^+ cation) of these ions. TEA^+ and BF_4^- ions form contact ion pairs in bulk ACN solution.

The structure and capacitance of the EDLs at the interface of organic electrolytes consisting of $TEABF_4$–ACN and model electrodes were also studied using MD simulations. The results indicate that:

1. Near neutral electrodes, the double-layer structure in the organic electrolyte is not a homogeneous mixture of ions and solvent as expected from classical continuum theories, but exhibits a number of notable features: the solvent shows strong layering and orientational ordering, ions are significantly contact-adsorbed on the electrode, and alternating layers of cations/anions penetrate about 1.1 nm into the bulk electrolyte. Although some of these features can also be observed in aqueous electrolytes, the significant contact-adsorption of ions and the alternating layering of cation/anion are new features found for EDLs in organic electrolytes. These features essentially originate from the fact that van der Waals interactions between the organic ions and electrode are strong and the partial desolvation of these ions occurs easily, both of which stems from the large size of the organic ions.

2. Near charged electrodes, distinct counter-ion concentration peaks, corresponding to the contact adsorption of counter-ions, are observed and the alternating layering of counter-ion/co-ion remains. The ion distribution cannot be described by the Helmholtz or Helmholtz + PB models because the number of counter-ions adsorbed on the electrode exceeds the electron charge on the electrode, and electrode is over-screened in part of the EDL. At $\sigma = \pm 0.105$ C m^{-2}, the counter-ions adsorbed on the electrode are partly desolvated in directions parallel to the electrode. The orientation of ACN molecules in the first ACN layer adjacent to the electrode is consistent with that expected from simple electrostatic theories, and the orientational ordering of ACN molecules becomes weak beyond the first ACN layer. The capacitance of the EDLs was determined to vary from 0.065 F m^{-2} to 0.092 F m^{-2} as the electrode charge density changes from -0.105 C m^{-2} to $+0.105$ C m^{-2}, in good agreement with that inferred from experimental measurements.

The rotation of interfacial ACN molecules is slowed down and this becomes more significant as the electrode is electrified. Retardation of the rotation of interfacial ACN molecules shows an asymmetric dependence on the sign of the electrode charge and was understood as a result of different ACN–ion interactions near electrodes with different signs of surface charge density. The diffusion of interfacial ACN, TEA^+, and BF_4^- ions is strongly anisotropic with the diffusion in directions parallel to the electrode ($D_{//}$) much larger than that in the direction normal to the electrode ($D_\perp$). $D_{//}$ of the interfacial ACN generally decreases as the magnitude of the electrode charge density increases. Similar to the rotational motion, the translational diffusion of interfacial ACN molecules also shows asymmetrical dependence on the sign of electrode charge. $D_{//}$ of interfacial ions has much less dependence on the magnitude of the electrode charge density. For BF_4^- anions adsorbed on their positive electrode, their diffusion coefficient is higher than that in the bulk because their motion near the charged electrode is less constrained by their pairing formed with TEA^+ cations. The rotation/diffusion of ACN and the diffusion of ions in the region beyond the first ACN or ion layer differ only weakly from those in the bulk.

Acknowledgements

The authors thank the Clemson-CCIT office for providing computer time. The Clemson authors acknowledge support from NSF under grant No. CBET-0756496. R.Q. was partly supported by an appointment to the HERE program for faculty at the Oak Ridge National Laboratory (ORNL) administered by ORISE. The authors at ORNL gratefully acknowledge the support from the Laboratory Directed Research and Development Program of ORNL and from U.S. Department of Energy under Contract No. DEAC05-00OR22725 with UT-Battelle, LLC at ORNL.

References

1 US Department of Energy, Basic research needs for electrical energy storage: report of the basic energy sciences workshop on electrical energy storage, (http://www.sc.doe.gov/bes/reports/files/EES_rpt.pdf), 2007.
2 (*a*) B. E. Conway, *Electrochemical Supercapacitors: Scientific Fundamentals and Technological Applications*, Kluwer Academic/Plenum, New York, 1999; (*b*) M. Winter and R. J. Brodd, *Chem. Rev.*, 2004, **104**, 4245–4269; (*c*) R. Kötz and M. Carlen, *Electrochim. Acta*, 2000, **45**, 2483–98; (*d*) A. Burke, *J. Power Sources*, 2000, **91**, 37–50.
3 J. R. Miller and P. Simon, *Science*, 2008, **321**, 651–52.
4 (*a*) P. Simon and Y. Gogotsi, *Nat. Mater.*, 2008, **7**, 845–54; (*b*) L. L. Zhang and X. S. Zhao, *Chem. Soc. Rev.*, 2009, **38**, 2520–2531.
5 A. G. Pandolfo and A. F. Hollenkamp, *J. Power Sources*, 2006, **157**, 11–27.
6 E. Frackowiak, *Phys. Chem. Chem. Phys.*, 2007, **9**, 1774–85.
7 (*a*) C. O. Ania, J. Pernak, F. Stefaniak, E. Raymundo-Piñero and F. Béguin, *Carbon*, 2009, **47**, 3158–3166; (*b*) R. Mysyk, E. Raymundo-Piñero, J. Pernak and F. Béguin, *J. Phys. Chem. C*, 2009, **113**, 13443–13449.
8 (*a*) C. Portet, Z. Yang, Y. Korenblit, Y. Gogotsi, R. Mokaya and G. Yushin, *J. Electrochem. Soc.*, 2009, **156**, A1–A6; (*b*) H. Nishihara, H. Itoi, T. Kogure, P. X. Hou, H. Touhara, F. Okino and T. Kyotani, *Chem.–Eur. J.*, 2009, **15**, 5355–5363; (*c*) T. E. Rufford, D. Hulicova-Jurcakova, E. Fiset, Z. H. Zhu and G. Q. Lu, *Electrochem. Commun.*, 2009, **11**, 974–977; (*d*) P. W. Ruch, R. Kotz and A. Wokaun, *Electrochim. Acta*, 2009, **54**, 4451–4458; (*e*) J. A. Fernandez, M. Arulepp, J. Leis, F. Stoeckli and T. A. Centeno, *Electrochim. Acta*, 2008, **53**, 7111–7116; (*f*) A. Janes and E. Lust, *J. Electrochem. Soc.*, 2006, **153**, A113–A116.
9 (*a*) P. Kurzweil and M. Chwistek, *J. Power Sources*, 2008, **176**, 555–567; (*b*) I. Nicotera, G. D. McLachlan, G. D. Bennett, I. Plitz, F. Badway, G. G. Amatucci and S. G. Greenbaum, *Electrochem. Solid-State Lett.*, 2007, **10**, A5–A8; (*c*) M. S. Ding, K. Xu, J. P. Zhang and T. R. Jow, *J. Power Sources*, 2004, **138**, 340–350; (*d*) K. Xu, S. P. Ding and T. R. Jow, *J. Electrochem. Soc.*, 1999, **146**, 4172–4178; (*e*) M. Ue, K. Ida and S. Mori, *J. Electrochem. Soc.*, 1994, **141**, 2989–2996.
10 (*a*) E. J. Lust, K. K. Lust and A. A. J. Janes, *Russ. J. Electrochem.*, 1995, **31**, 807–821; (*b*) S. I. Lee, K. Saito, K. Kanehashi, M. Hatakeyama, S. Mitani, S. H. Yoon, Y. Korai and I. Mochida, *Carbon*, 2006, **44**, 2578–2586.
11 (*a*) M. R. Philpott, J. N. Glosli and S. B. Zhu, *Surf. Sci.*, 1995, **335**, 422–431; (*b*) E. Spohr, *Electrochim. Acta*, 1999, **44**, 1697–1705; (*c*) D. I. Dimitrov, N. D. Raev and K. I. Semerdzhiev, *Phys. Chem.*

Chem. Phys., 2001, **3**, 448–452; (*d*) C. Cagle, G. Feng, R. Qiao, J. Huang, B. G. Sumpter and V. Meunier, *Microfluid. Nanofluid*., 2009, DOI: 10.1007/s10404-009-0542-2.
12 L. Yang, B. H. Fishbine, A. Migliori and L. R. Pratt, *J. Am. Chem. Soc*., 2009, **131**, 12373–12376.
13 N. D. Lang and W. Kohn, *Phys. Rev. B: Solid State*, 1971, **3**, 1215–1223.
14 A. V. Raghunathan and N. R. Aluru, *Phys. Rev. E: Stat., Nonlinear, Soft Matter Phys*., 2007, **76**, 011202.
15 W. D. Cornell, P. Cieplak, C. I. Bayly, I. R. Gould, K. M. Merz, D. M. Ferguson, D. C. Spellmeyer, T. Fox, J. W. Caldwell and P. A. Kollman, *J. Am. Chem. Soc*., 1995, **117**, 5179–5197.
16 J. M. Wang, R. M. Wolf, J. W. Caldwell, P. A. Kollman and D. A. Case, *J. Comput. Chem*., 2004, **25**, 1157–1174.
17 V. B. Luzhkov, F. Osterberg, P. Acharya, J. Chattopadhyaya and J. Aqvist, *Phys. Chem. Chem. Phys*., 2002, **4**, 4640–4647.
18 X. Wu, Z. Liu, S. Huang and W. Wang, *Phys. Chem. Chem. Phys*., 2005, **7**, 2771–2779.
19 *CRC Handbook of Chemistry and Physics*, Internet Version 2010, ed. D. R. Lide and W. M. "Mickey" Haynes, CRC Press, Boca Raton, FL, 90th edn, 2009, pp. 6–148.
20 E. Lindahl, B. Hess and D. van der Spoel, *J. Mol. Model*., 2001, **7**, 306–317.
21 I. Yeh and M. Berkowitz, *J. Chem. Phys*., 1999, **111**, 3155–3162.
22 B. Hess, H. Bekker, H. J. C. Berendsen and J. G. E. M. Fraaije, *J. Comput. Chem*., 1997, **18**, 1463–1472.
23 R. Qiao and N. R. Aluru, *Colloids Surf., A*, 2005, **267**, 103–109.
24 A. V. Marenich, R. M. Olson, C. P. Kelly, C. J. Cramer and D. G. Truhlar, *J. Chem. Theory Comput*., 2007, **3**, 2011–2033.
25 M. Higashi, A. V. Marenich, R. M. Olson, A. C. Chamberlin, J. Pu, C. P. Kelly, J. D. Thompson, J. D. Xidos, J. Li, T. Zhu, G. D. Hawkins, Y.-Y. Chuang, P. L. Fast, B. J. Lynch, D. A. Liotard, D. Rinaldi, J. Gao, C. J. Cramer and D. G. Truhlar, *GAMESSPLUS—version 2009*, University of Minnesota, Minneapolis, 2009.
26 General Atomic and Molecular Electronic Structure System (GAMESS), April 11, 2008 R1 version; M. W. Schmidt, K. K. Baldridge, J. A. Boatz, S. T. Elbert, M. S. Gordon, J. H. Jensen, S. Koseki, N. Matsunaga, K. A. Nguyen, S. J. Su, T. L. Windus, M. Dupuis and J. A. Montgomery, *J. Comput. Chem*., 1993, **14**, 1347–1363.
27 C. P. Kelly, C. J. Cramer and D. G. Truhlar, *J. Chem. Theory Comput*., 2005, **1**, 1133–1152.
28 V. B. Luzhkov, F. Österberg, P. Acharya, J. Chattopadhyaya and J. Åqvist, *Phys. Chem. Chem. Phys*., 2002, **4**, 4640–4647.
29 A. V. Marenich, C. P. Kelly, J. D. Thompson, G. D. Hawkins, C. C. Chambers, D. J. Giesen, P. Winget, C. J. Cramer and D. G. Truhlar, *Minnesota Solvation Database—version 2009*, University of Minnesota, Minneapolis, 2009.
30 A. Ben-Naim, *Solvation Thermodynamics*, Plenum, New York, NY, 1987.
31 K. W. Frese, Jr., *J. Phys. Chem*., 1989, **93**, 5911–5916.
32 S. Rajamani, T. Ghosh and S. Garde, *J. Chem. Phys*., 2004, **120**, 4457–4466.
33 (*a*) M. Ue, *J. Electrochem. Soc*., 1994, **141**, 3336; (*b*) Y. Marcus, *Biophys. Chem*., 1994, **51**, 111; (*c*) H. D. B. Jenkins and K. P. Thakur, *J. Chem. Educ*., 1979, **56**, 576.
34 (*a*) J. Chmiola, C. Largeot, P. L. Taberna, P. Simon and Y. Gogotsi, *Angew. Chem., Int. Ed*., 2008, **47**, 3392–3395; (*b*) J. Chmiola, G. Yushin, Y. Gogotsi, C. Portet, P. Simon and P. L. Taberna, *Science*, 2006, **313**, 1760–1763.
35 H. Greberg and R. Kjellander, *J. Chem. Phys*., 1998, **108**, 2940–2953.
36 M. Maroncelli, *J. Chem. Phys*., 1991, **94**, 2084–2103.
37 R. M. Lynden-Bell, M. G. Del Popolo, T. G. A. Youngs, J. Kohanoff, C. G. Hanke, J. B. Harper and C. C. Pinilla, *Acc. Chem. Res*., 2007, **40**, 1138–1145.
38 A. Markovits and C. Minot, *Catal. Lett*., 2003, **91**, 225–234.
39 S. Baldelli, G. Mailhot, P. Ross, Y.-R. Shen and G. A. Somorjai, *J. Phys. Chem. B*, 2001, **105**, 654–662.
40 F. Schiffmann, J. Hutter and J. V. Vondele, *J. Phys.: Condens. Matter*, 2008, **20**, 064206.
41 J. N. Glosli and M. R. Philpott, *J. Chem. Phys*., 1992, **96**, 6962–6969.
42 (*a*) V. Meunier, S. V. Kalinin and B. G. Sumpter, *Phys. Rev. Lett*., 2007, **98**, 056401; (*b*) V. Meunier and B. G. Sumpter, *J. Chem. Phys*., 2005, **123**, 024705.
43 G. Feng, J. S. Zhang and R. Qiao, *J. Phys. Chem. C*, 2009, **113**, 4549–4559.
44 J. Huang, B. G. Sumpter and V. Meunier, *Chem.–Eur. J*., 2008, **14**, 6614–6626.
45 W. Schmickler and D. Henderson, *Prog. Surf. Sci*., 1986, **22**, 323–419.
46 J. W. Halley, *Electrochim. Acta*, 1996, **41**, 2229–2251.
47 L. A. Pozhar, *Transport Theory of Inhomogeneous Fluids*, World Scientific Press, Singapore, 1994.